Final Draft
of the original manuscript:

Srinivasan, P.B.; Riekehr, S.; Blawert, C.; Dietzel, W.; Kocak, M.:
Slow strain rate stress corrosion cracking behaviour of as-welded and plasma electrolytic oxidation treated AZ31HP magnesium alloy autogenous laser beam weldment
In: Materials Science and Engineering A (2009) Elsevier

DOI: 10.1016/j.msea.2009.03.069

Slow strain rate stress corrosion cracking behaviour of as-welded and plasma electrolytic oxidation treated AZ31HP magnesium alloy autogenous laser beam weldment

P. Bala Srinivasan*, S. Riekehr , C. Blawert, W. Dietzel, M. Koçak
Institute of Materials Research
GKSS-Forschungszentrum Geesthacht GmbH
D-21502 Geesthacht, Germany

*Corresponding Author (bala.srinivasan@gkss.de);
Phone: 00-49-4152-871997; Fax: 00-49-4152-871909

Key words:
Magnesium alloy; Laser welding; Microstructure; Mechanical properties; Slow strain rate tensile test; Stress corrosion cracking; Fractography.

*Corresponding Author (bala.srinivasan@gkss.de)

Abstract

The joining of a thin section AZ31HP magnesium alloy was accomplished by laser beam welding in the autogenous mode using a Nd-YAG laser system. Micro hardness evaluation and the slow strain rate tensile (SSRT) tests in air revealed that the weld metal had near-matching mechanical properties corresponding to that of the parent alloy. However, in terms of stress corrosion cracking (SCC) resistance as assessed by SSRT tests in ASTM D1384 solution, the weldment was found to have higher susceptibility compared to the parent alloy. The fracture in the weld metal/fusion boundary/HAZ interface suggested that the failure was due to the grain coarsening at the very narrow heat affected zone. The resistance to SCC of the parent alloy and the weldment specimens was found to improve slightly by the application of plasma electrolytic oxidation (PEO) coating from a silicate based electrolyte.

Introduction

Light weight wrought magnesium alloys are candidate materials for some of the automotive and aerospace applications owing to their excellent property combinations. Joining of magnesium alloys is widely contemplated by gas tungsten arc welding [1-3],

and laser beam welding is increasingly used due to its novel features and flexibility of operations [4-5]. Even though both CO_2 and Nd-YAG lasers can be used for joining of magnesium alloys, the latter has been reported to be better in terms of welding efficiency and deeper penetration capabilities [6-7]. A few recent publications on laser welding of wrought magnesium alloys suggest the effectiveness of laser welding technique to achieve near-matching mechanical properties for the weldments as that of the parent alloy [8-9].

Magnesium alloys with an active potential in the electromotive force series, possess a poor corrosion resistance [10-11]. The corrosion behaviour of weldments of magnesium alloys have been reported to be influenced by the grain size and microstructural variations in the weld metal and heat affected zone and further by the compositional variations due to effects of segregation [12-13]. A wide range of surface treatments are available for combating the corrosion problems [14-15] and amidst that the plasma electrolytic oxidation (PEO) process is gaining popularity in recent times [16-18]. For many critical applications the resistance to stress corrosion cracking (SCC) becomes an important criterion, and magnesium alloys have been reported to be highly susceptible to cracking in various environments including distilled water [19-23]. Recently, a few attempts have been made to understand the effects of PEO coating on the SCC resistance of magnesium alloy and also its friction stir weldment, as the PEO coating was expected to delay the onset of corrosion and consequent cracking [24-26]. Since there is not much published information on the stress corrosion cracking of magnesium alloy weldments except a few from the authors' research group [27-29], the current investigation was aimed at the characterisation of an autogenous laser weldment of AZ31HP magnesium alloy for microstructure, mechanical properties and stress corrosion cracking (SCC) behaviour. In addition, the parent alloy and the weldment

specimens were subjected to plasma electrolytic oxidation treatment and the effect of the PEO coating on the SCC resistance was studied.

Experimental

The raw material for this investigation was in the form of rolled sheets of 2.5 mm thickness corresponding to AZ31HP magnesium alloy with a nominal chemical composition of 2.5 – 3.5 wt% Al, 0.6 – 1.4 wt% Zn, 0.2 – 0.6 wt% Mn, balance Mg. A Nd-YAG laser system was employed for joining the sheets (size: 200 mm x 330 mm x 2.5 mm each) in the form of a butt joint without filler wire (autogenous mode). The welding was performed along the rolling direction of the sheets. The following optimized welding parameters were chosen for producing the final welds: laser power 2.2 kW; welding speed 90 $mm \cdot s^{-1}$; focus on surface; helium shielding 16 $L \cdot min^{-1}$ (top side), 40 $L \cdot min^{-1}$ (bottom side). No post-weld heat treatment was done and the weldment was characterized in the as-welded condition.

The metallographic specimens (cross-sections) were polished successively with 500, 1200 and 2500 grit emery sheets followed by final polishing with OP-S and etched in a solution containing 3.5 g picric acid, 6.5 ml acetic acid, 20 ml water and 100 ml ethanol. Microstructural examination was performed with a Leitz optical microscope and Cambridge Stereoscan 200 scanning electron microscope (SEM). Microhardness evaluation across the weldment was carried out under a load of 100 g with a loading dwell time of 20 s.

The plasma electrolytic oxidation (PEO) of the parent alloy and the weldment specimen was carried out in a silicate based alkaline electrolyte using a DC power source at a constant current density of 150 $A \cdot m^{-2}$ for 30 minutes. All the specimens were ground to 1200 grit emery finish and cleaned with acetone prior to the treatment. Coating

thickness measurements were made using a non-destructive test probe (Minitest 2100), and the surface morphology of the PEO coating was examined in SEM.

The SCC susceptibility of the parent alloy and the weldment was assessed by slow strain rate tensile tests (SSRT) in ASTM D 1384 solution containing 148 $mg \cdot L^{-1}$ Na_2SO_4, 165 $mg \cdot L^{-1}$ NaCl and 138 $mg \cdot L^{-1}$ $NaHCO_3$ in 1 L of distilled water at a nominal strain rate of 10^{-6} s^{-1} by following the ISO standard 7359—Part 7 [30]. The parent alloy was tested in the longitudinal direction (parallel to the rolling direction of the sheet) and the weldment specimen was assessed in the transverse direction. The schematic representation of the geometry of the specimens employed for SSRT tests is presented in Figure 1. Both the parent and weldment specimens in the untreated condition were ground to 1200 grit emery finish before the SSRT tests whereas the PEO coated specimens were used in the as-coated condition. Reference tests were performed in air under similar strain rate. The elongation of the specimens in the SSRT tests (in air and in ASTM solution) was measured by employing two linear variable displacement transducers (LVDTs) attached to the specimen grips. The specimens after the SSRT tests were examined in the light microscope, and fracture surface analysis was done in the SEM.

Results and Discussion

Microstructure and Microhardness

The optical macrograph of the laser weldment shown in Figure 2 reveals a wine-glass shaped bead with a maximum width of approximately 2 mm at the face region of the weld and 1 mm at the root. As is expected in a laser weldment, no distinct heat affected zone is visible in this macrograph. However, the weld bead contained a few tiny pores, which are characteristic in laser beam magnesium alloy welds.

The scanning electron micrographs of the different regions of the weldment are depicted in Figures 3(a), (b) and (c). A mixed grain structure (equiaxed, polygonal and elongated grains) with small distribution of ß-phase was observed in the parent alloy (Figure 3(a)). Figure 3(b) shows the microstructure of the heat affected zone (HAZ) – weld metal interface. The heat affected zone was very narrow (roughly <100 μm on either side of the weld metal), and this was constituted by large polygonal grains with an average grain size of 20 μm. The weld metal had a fine grained, polygonal structure (Figure 3(c)), with an average grain size of <10 μm. In addition, a large number of fine particles of size <1 μm were present in the weld metal and was found to be spread uniformly across the matrix. Kannan et al., [23] and Chi et al., [31] in their recent publications have observed the formation such particles in the laser beam and electron beam weld metals of AZ31 magnesium alloy, respectively. Coehlo et al., [8] also have reported the presence of fine particles in AZ31 magnesium alloy laser weld metal, and identified them as $Mg_{17}(Al,Zn)_{12}$ by TEM diffraction patterns. EDS analysis performed in the current investigation showed that these particles were richer in Al, Zn compared to the parent alloy, suggesting that these also could only be $Mg_{17}(Al,Zn)_{12}$ phase, formed due to the rapid cooling rates associated with the high energy density – low heat input conditions experienced during laser welding.

Micro hardness measurements made across the weldment showed hardness values of 70 ± 10 $HV_{0.1}$ in the entire weldment (parent, HAZ and weld metal regions). Neither the slight grain coarsening in the HAZ nor the evolution of a fine grain sized weld metal seemed to influence the hardness values in these regions. Further, the ß-phase particles in the weld metal also did not contribute to hardness. Even though some researchers claimed an increase in hardness in the weld metal due to fine grained structure and the presence of intermetallic compounds in the welds of cast magnesium alloys [32-34], many of the publications on the laser welding of wrought alloys have

reported that there was no appreciable change in the hardness in different regions of the weldments [8, 23, 34-35].

Slow strain rate tensile behaviour

The SSRT tests (strain rate: 10^{-6} s^{-1}) performed in air showed that both the parent alloy and the weldment specimen have similar ultimate strength levels of around 250 MPa. The elongation values measured in these tests did not represent the precise strain levels of the specimens as the measurement was done with two LVDTs fitted to the specimen grips. However, they can be used qualitatively to understand the ductility of the weldment, and in the following discussion section it is referred to as "apparent strain". The weldment specimen showed an apparent strain value of 45.5% as against a value of 57% registered for the parent alloy. It is well known that the weldments when tested in the transverse direction (with the composite zone comprising weld metal, HAZ and parent alloy in the gauge section), undergo different levels of straining in the regions mentioned above, and hence the strain measured may not represent the true ductility. However, the reduction in cross-sectional area (RA) values showed a similar trend as that of apparent strain, registering values of 48.9% and 30.9%, for the parent and weldment specimens, respectively, suggesting that the weldment has a lower ductility compared to the parent alloy.

Figure 4(a) shows the optical macrograph of the weldment specimen SSRT tested in air. The reduction in the section thickness in the weld metal region, leading to necking and fracture is evident in this macrograph. The higher magnification micrograph (Figure 4(b)) obtained from the face region of the weld shows that the specimen had fractured along the HAZ region near to the fusion boundary. It is interesting that the weld metal showed good mechanical properties despite the presence of isolated small pores. It appears that the weld metal and fusion boundary/HAZ were the weakest regions in this weldment, hence the deformation and the consequent fracture had

occurred in these regions. The weld metal region with a fine-grained structure probably had a better ductility comparable to that of the parent alloy. However, the early fracture and relatively low values of ductility parameters viz., apparent strain and RA observed for the weldment can be attributed to the damage initiation and growth in the coarse grained HAZ, as is evident in Figures 4(a) and (b).

The scanning electron fractographs of the parent alloy and the weldment specimens shown in Figures 5(a) and (b), respectively, reveal a dimpled fracture surface, characteristic of ductile fracture. Even though the dimples seen inside the grains in both cases were of fine size, the grain facets appear larger in the weldment specimen, which corroborate the fact that the fracture was along the relatively coarse grained HAZ in this specimen. Nevertheless, the micro hardness survey and the SSRT test data suggest that this autogenous laser weldment, as a whole, has similar mechanical properties as that of the parent alloy with a high joint efficiency.

Stress corrosion cracking

In the SSRT tests performed in ASTM D1384 solution at a nominal strain rate of 10^{-6} s^{-1}, the parent alloy had fractured at a stress level of 195 MPa with an apparent strain value of 6.1%. For the weldment specimen the fracture was noticed at a marginally lower stress (185 MPa) with an apparent strain value of 4.7%. The RA observed in the parent and weldment specimens were 7.8% and 7.5%, respectively. A much higher degree of susceptibility to SCC was observed and reported for AZ31 magnesium alloy [23] in the SSRT tests at lower strain rates of 10^{-8} s^{-1} and 10^{-7} s^{-1} for the laser and friction stir weldments, respectively. However, in this work the SSRT tests were performed intentionally at a higher strain rate in order to understand the SCC behaviour. The fact that these specimens have failed at a lower stress level and that the apparent strain and RA values were extremely low compared to their counterparts tested in air demonstrates their SCC susceptibility in ASTM solution even at this higher strain rate.

The optical macrograph of the SSRT tested weldment specimen in ASTM D1384 solution is shown in Figure 6(a). Even though a crack was observed in the parent alloy, the specimen had failed in the weld metal/HAZ region. The deformation of the weld metal as a result of straining can be seen in the root region of this weldment. It may appear from this macrograph that the fracture was along the fusion boundary/HAZ as was observed in the case of the test in air. But, the higher magnification micrograph obtained from the face region of the weld shown in Figure 6(b) reveals that the crack initiation was in the weld metal near to the fusion line. A closer examination of this fractured specimen showed a crack in the weld metal in the root region (Figure 6(c)) as well, and this observation further reaffirms the fact that the weld metal has a higher susceptibility to SCC in this weldment. It is probable that during the straining/ deformation of the weld metal, micro cracks had developed on the surface, due to the cracking of surface oxide/hydroxide layers, which subsequently might have led to the propagation of crack and premature fracture. The scanning electron fractographs of the parent and weldment specimens shown in Figures 7(a) and (b), respectively, reveal a brittle fracture in transgranular mode in both the cases. The fracture surface of the weldment specimen looks a little different from that of the parent, and this was possibly the result of the inadvertent longer exposure of the fractured specimen to the SCC test electrolyte after the tests.

Effect of plasma electrolytic oxidation coating on the SCC behaviour

In order to understand the effect of surface modification on the stress corrosion cracking behaviour the parent alloy and the weldment, the plasma electrolytic oxidation (PEO) treatment was carried out. The PEO coatings have been reported to offer an excellent resistance to general corrosion in aqueous environments [36-37]. A representative scanning electron micrograph of the PEO coated parent alloy specimen showing the surface morphology is presented in Figure 8. The characteristic porous surface with

pore diameters in the range 0.5 μm to 10 μm can be observed from this micrograph. The surface morphologies of the different regions of PEO treated weldment were very similar to that of the parent alloy, and the thickness of the coating was 16 ± 2 μm in both the parent and weldment specimens.

In the SSRT tests in ASTM solution, the PEO coated parent alloy has failed at a stress of 205 MPa with an apparent strain of 12.7% and a RA of 9.5%. The corresponding stress, elongation and RA values for the PEO coated weldment specimen were 205 MPa, 10.7% and 9.5%, respectively. Even though the PEO coated specimens lasted a longer duration in the SSRT tests, there was no apparent improvement in the SCC behaviour in terms of maximum stress to fracture. In the context of total strain, there appears to be an appreciable influence in the presence of PEO coating. Under constantly increasing stress in the SSRT tests, the PEO coating was found to develop transverse cracks perpendicular to the loading direction (Figure 9). The development of such cracks retards the strain hardening behaviour of the alloy. Thus, with the failure of coating at many locations, cracks initiate and even at this lower stress level the cracks begin to open up, showing higher strain values. Apparently, the mechanism was found to change from material deformation to crack opening in the specimens with PEO coating. A similar observation was reported in a work on PEO coated AM50 cast magnesium alloy assessed for SCC behaviour by SSRT tests [38].

The optical macrograph of the SSRT tested PEO coated weldment specimen shown in Figure 10(a) reveals that the fracture in this case was in the HAZ with the crack path through the weld metal/HAZ regions. This further confirms that the cracking of the surface layers in the strained regions of the HAZ/weld metal was responsible for the initiation of cracks for SCC. Apparently, this weld metal/HAZ region was undergoing deformation, and as the cracks began to open up, the electrolyte was getting into the substrate to cause more corrosion damage. The higher susceptibility of the HAZ/weld

metal region to SCC even in the coated condition is illustrated by the higher magnification micrographs in Figure 10(b) and (c). The presence of a crack in the HAZ close to the root region of weld suggests that the weld metal to be the vulnerable region for SCC (Figure 10(d)).

The fracture surface of the SSRT tested PEO coated specimens had very similar features as that of the SSRT tested untreated specimens (in ASTM solution), and a representative fractograph of the PEO coated specimen is depicted in Figure 11. Even though the RA and apparent strain values were marginally higher, the fracture surface appearance was quite brittle, suggesting that the PEO treatment did not prevent the SCC of this parent alloy/weldment in ASTM D1384 solution even at this higher strain rate. It had already been demonstrated in a recent work that the PEO coatings do not influence the SCC behaviour of AZ61 wrought magnesium alloy in ASTM D 1384 solution [25]. It, however, remains to be seen as to how this parent alloy and the weldment with and without the PEO treatment behave in the constant load SCC tests at stress levels below the yield strength.

Conclusions

Autogenous laser welds with matching mechanical properties to that of the parent magnesium alloy could be obtained by Nd-YAG welding. The laser weldment has exhibited a higher susceptibility to SCC in ASTM solution when SSRT tested at a strain rate of 10^{-6} s^{-1}. The PEO treatment could bring an improvement in SCC resistance of both the parent alloy and laser weldment in terms of time to fracture. However, the SCC is retarded only until the strain causes the coating to fail. The cracking of the coating and the resultant seepage of electrolyte into the substrate were responsible for the SCC of PEO coated parent and weldment specimens. In the laser weldment specimen, the narrow HAZ and the weld metal region adjoining the fusion boundary were found to exhibit a higher sensitivity to stress corrosion crack initiation and growth.

Acknowledgement

The authors express their sincere thanks to Mr. Ulrich Burmester, Mr. Volker Heitmann and Mr. Volker Kree for the technical support during the course of this work. PBS thankfully acknowledges the Alexander von Humboldt Foundation, Germany and DAAD, Germany for the award of research fellowships.

References

1. A. Munitz, C. Cotler, A. Stern, G. Kohn, Materials Science and Engineering, A302 (2001) 68.

2. L.M. Liu, D.H. Cai, Z.D. Zhang, Scripta Materialia, 57 (2007) 695.

3. L. Liu, C. Dong, Materials Letters, 60 (2006) 2194.

4. X. Cao, M. Jahazi, J.P. Immarigeon, W. Wallace, Journal of Materials Processing Technology, 171 (2006) 188.

5. Y.J. Quan, Z.H. Chen, X.S. Gong, Z.H. Yu, Materials Characterisation, 59 (2008) 1491.

6. K.G. Watkins, in: H.I. Kaplan (Ed.), Laser welding of magnesium alloys, Magnesium Technology 2003, TMS Annual Meeting and Exhibition, San Diego, CA, 2-6 March, 2003, pp 153-156.

7. H. Haferkamp, U. Dilthey, G. Trager, I. Burmester, M. Niemeyer, Beam welding of magnesium alloys, in: Proceedings Confrence: Magnesium Alloys and their Applications, Wolfsburg, Germany, 28-30 April, 1998, pp 595-600.

8. R.S. Coelho, A. Kostka, H. Pinto, S. Riekehr, M. Koçak, A.R. Pyzalla, Materials Science and Engineering, A485 (2008) 20.

9. V. Ventzke, S. Riekehr, M. Koçak, Materials Science and Engineering Technology, 39 (2008) 435.

10. G. Song, A. Atrens, Advanced Engineering Materials, 1 (1999) 11.

11. E. Ghali, Magnesium and Magnesium alloys, in Uhlig's Corrosion Handbook, R.W. Revie, ed., John Wiley, New York, 2000, Ch. 44, pp.793–830.

12. G. Ben-Hamua, D. Eliezer, C.E. Cross, Th. B¨ollinghaus, Materials Science and Engineering, A452–453 (2007) 210.

13. Y.H. Jang, S.S. Kim, C. D. Yim, C.G. Lee and S.J. Kim, Corrosion Engineering Science and Technology, 42 (2007) 119.

14. C. Blawert, W. Dietzel, E. Ghali, G. Song, Advanced Engineering Materials, 8 (2006) 511.

15. J.E. Gray, B. Luan, Journal of Alloys and Compounds, 336 (2002) 88.

16. J. Liang, T. Hu, J. Hao, Applied Surface Science, 253 (2007) 4490.

17. Q. Cai, L. Wang, B. Wei, Q. Liu, Surface and Coatings Technology, 200 (2006) 3727.

18. P. Bala Srinivasan, J. Liang, C. Blawert, M. Störmer, W. Dietzel, Applied Surface Science, Accepted for publication, In press

19. N. Winzer, A. Atrens, W. Dietzel, V.S. Raja, G. Song, K.U. Kainer, Materials Science and Engineering, A488 (2008) 339.

20. M. Bobby Kannan, R.K. Singh Raman, Scripta Materialia, 59 (2008) 175.

21. R.G. Song, C. Blawert, W. Dietzel, A. Atrens, Materials Science and Engineering, A399 (2005) 308.

22. M. Bobby Kannan, W. Dietzel, C. Blawert, A. Atrens, P. Lyon, Materials Science and Engineering, A480 (2008) 529.

23. J. Chen, J. Wang, E. Han, W. Ke, Materials Science and Engineering, A488 (2008) 428.

24. P. Bala Srinivasan, C. Blawert, W. Dietzel, Materials Science and Engineering, A494 (2008) 401.

25. P. Bala Srinivasan, C. Blawert, W. Dietzel, Corrosion Science, 50 (2008) 2415.

26. P. Bala Srinivasan, R. Zettler, C. Blawert, W. Dietzel, Materials Characterisation, 60 (2009) 389.

27. M. Bobby Kannan, W. Dietzel, R. Zeng, R. Zettler, J.F. dos Santos, Materials Science and Engineering, A460-461 (2007) 243.

28. P. Bala Srinivasan, R. Zettler, C. Blawert, W. Dietzel, Corrosion Engineering Science and Technology, DOI 10.1179/174327808X315704.

29. M. Bobby Kannan, W. Dietzel, C. Blawert, S. Riekehr, M. Koçak, Materials Science and Engineering, A444 (2007) 220.

30. International Standard ISO 7539, Corrosion of metals and alloys—Stress corrosion testing; Part 7: Slow strain rate stress corrosion tests, International Organization for Standardization, Geneva, 1989.

31. C.T. Chi, C.G. Chao, T.F. Liu, C.C. Wang, Materials Science and Engineering, A435-436 (2006) 672.

32. A. Weisheit, R. Galun, B.L. Mordike, IIW Seminar, Trends in welding of light weight automobile railroad vehicles, 1997, 28-41.

33. M. Pastor, H. Zhao, T. Debroy, Journal of Laser Applications, 12 (2000) 91.

34. A. Weisheit, R. Galun, B.L. Mordike,Welding Journal, 74 (1998) 149.

35. P.G. Sanders, J.S. Keske, K.H.Leong, G. Kornecki, Journal of Laser Applications, 11 (1999) 96.

36. H. Duan, C. Yan, F. Wang, Electrochimica Acta, 52 (2007) 3785.

37. J. Liang, L. Hu, J. Hao, Applied Suface Science, 253 (2007) 4490.

38. P. Bala Srinivasan, C. Blawert, W. Dietzel, K.U. Kainer, Scripta Materialia, 59 (2008) 43.

Figure Captions

Figure 1 Schematic representation of tensile specimen used for SSRT tests

Figure 2 Optical macrograph of laser beam weldment

Figure 3 Scanning electron micrographs showing the microstructural features of different regions of the AZ31HP autogenous laser weldment

Figure 4 Optical macro/micrographs of the SSRT tested weldment specimen (in air)
(a) overview (arrow shows region of necking)
(b) fracture location in the face of weld metal (higher magnification of region marked (b) in (a)

Figure 5 Scanning electron fractographs of the SSRT tested specimens (in air)

Figure 6 Optical macro/micrographs of the SSRT tested weldment specimen (in ASTM D1384 solution)
(a) overview
(b) fracture location in the face region of weld metal
(c) crack in the weld metal in the root region

Figure 7 Scanning electron fractographs of the SSRT tested specimens (in ASTM D1384 solution)

Figure 8 Representative scanning electron micrograph showing the morphology of PEO coating on AZ31HP magnesium alloy

Figure 9 Optical macrograph showing the transverse cracks in the SSRT tested PEO coated parent alloy specimen

Figure 10 Optical macro/micrographs of the SSRT tested PEO coated weldment specimen
(a) overview (arrow shows the region of stress corrosion crack initiation)
(b) higher magnification micrograph of region marked in dotted square in (a)
(c) higher magnification micrograph of region marked in dotted square in (b)
(d) crack in the HAZ close to the fusion boundary in the root region of the weldment (marked in dotted square in (b))

Figure 11 Scanning electron fractograph of the SSRT tested (in ASTM solution) PEO coated parent alloy specimen

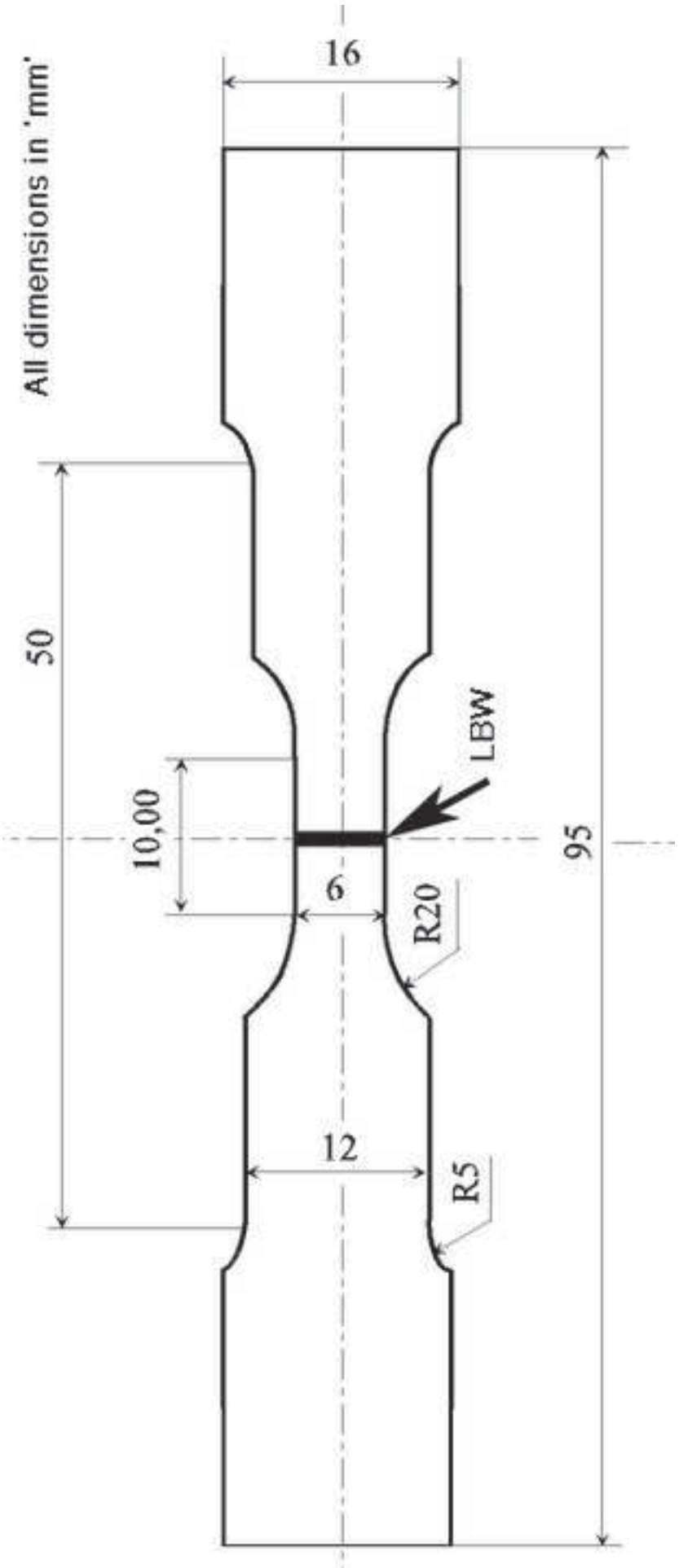

Figure 1
Click here to download high resolution image

Figure 2

Click here to download high resolution image

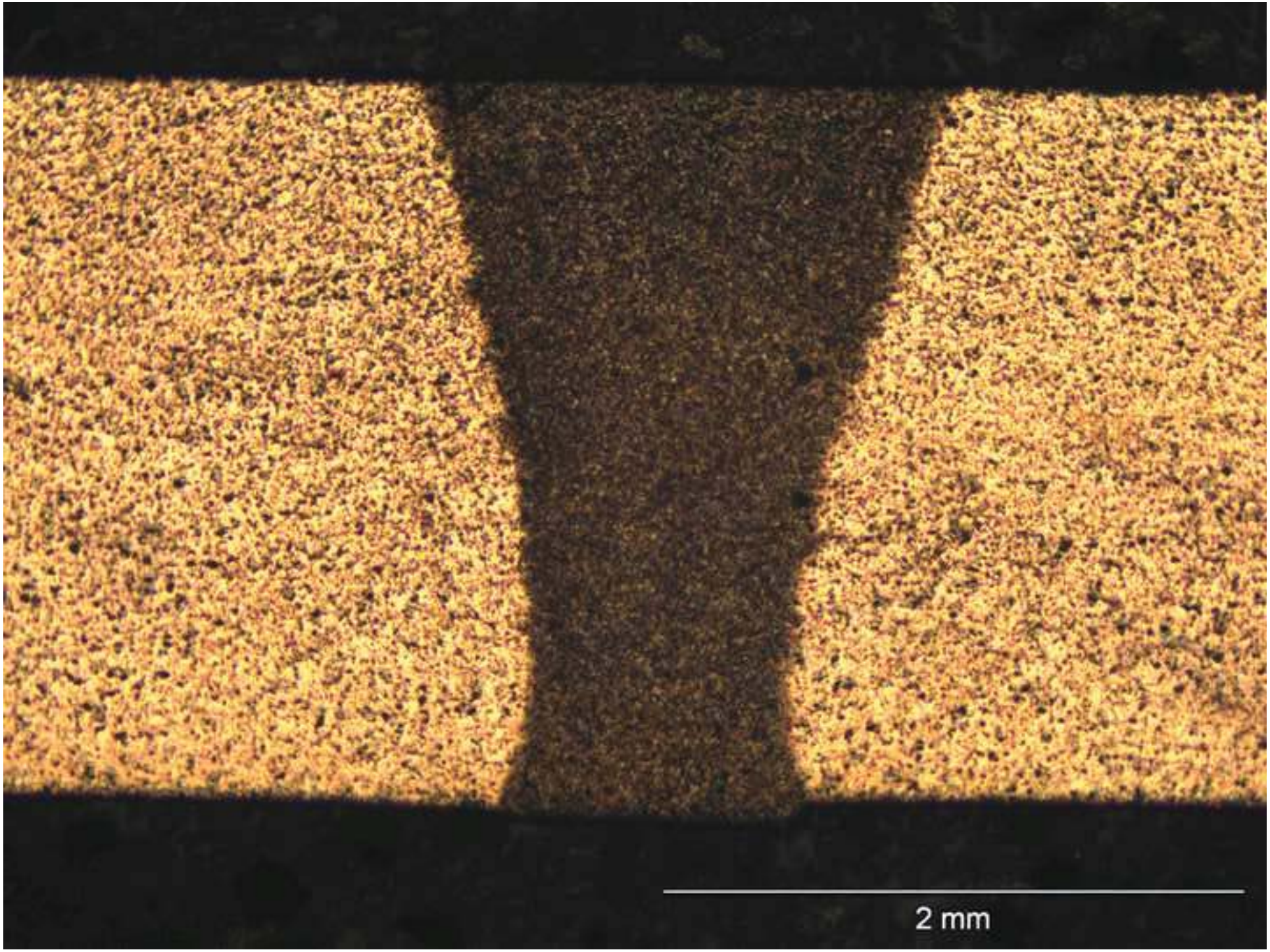

Figure 3a
Click here to download high resolution image

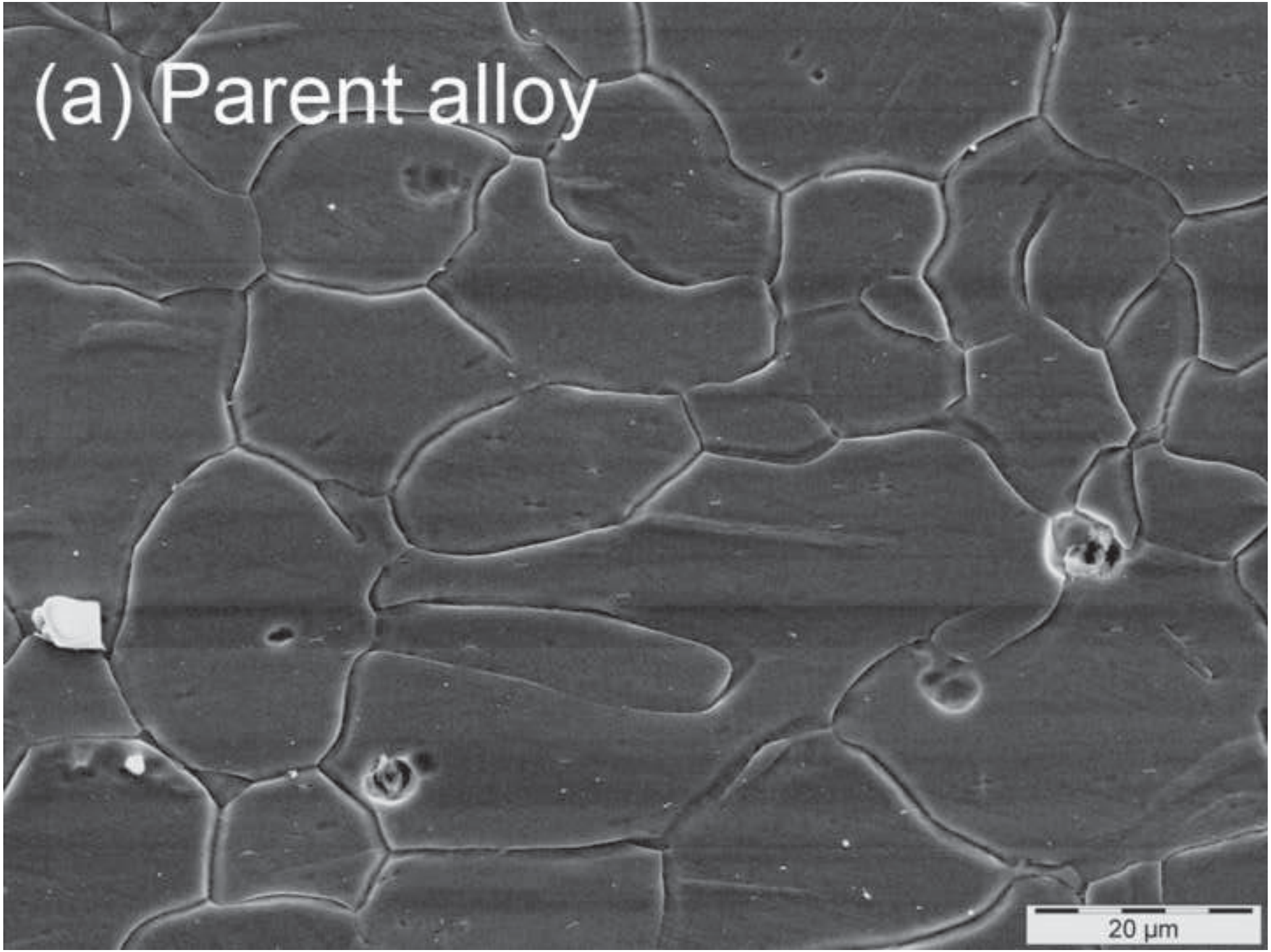

Figure 3b
Click here to download high resolution image

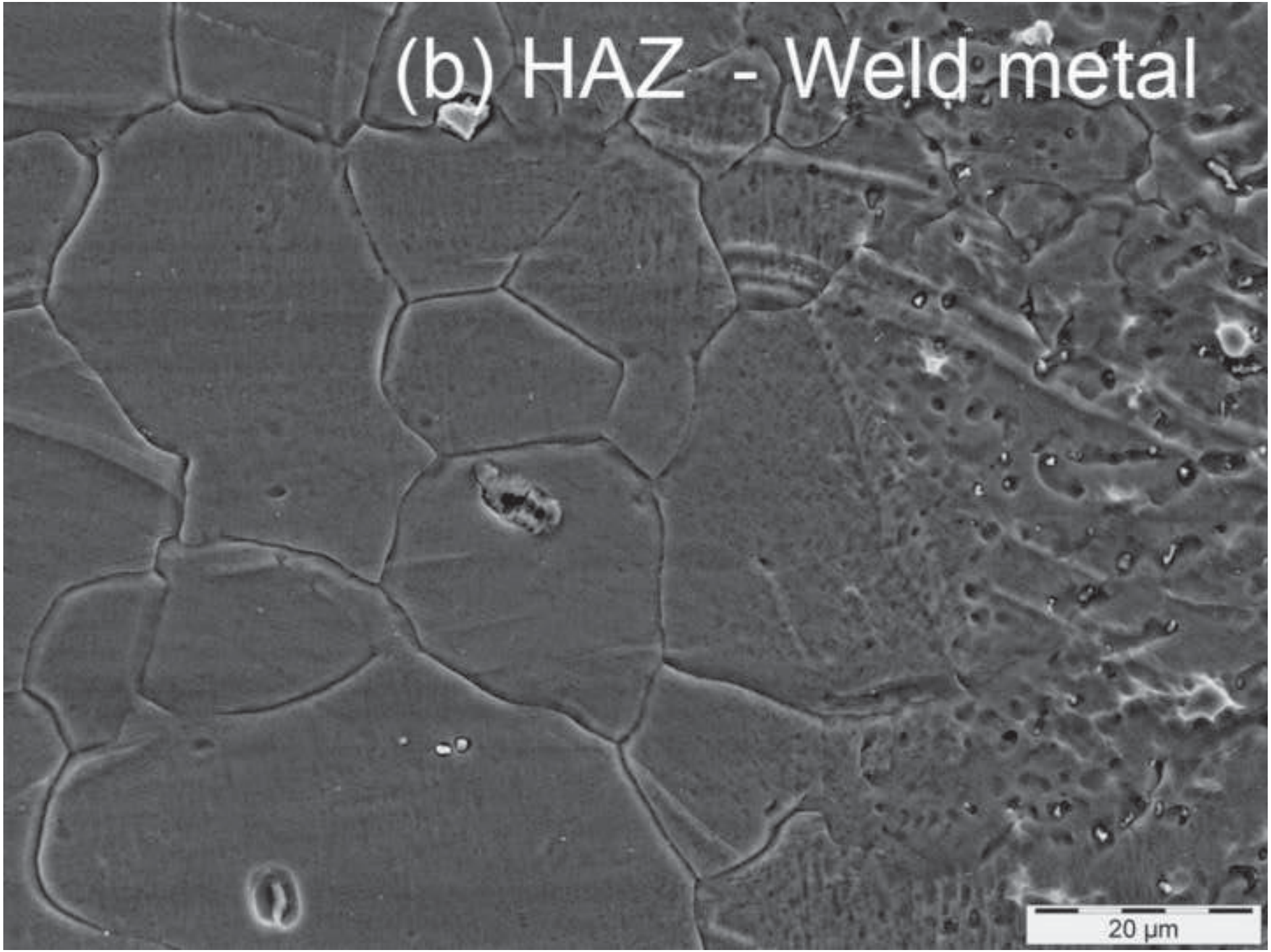

Figure 3c
Click here to download high resolution image

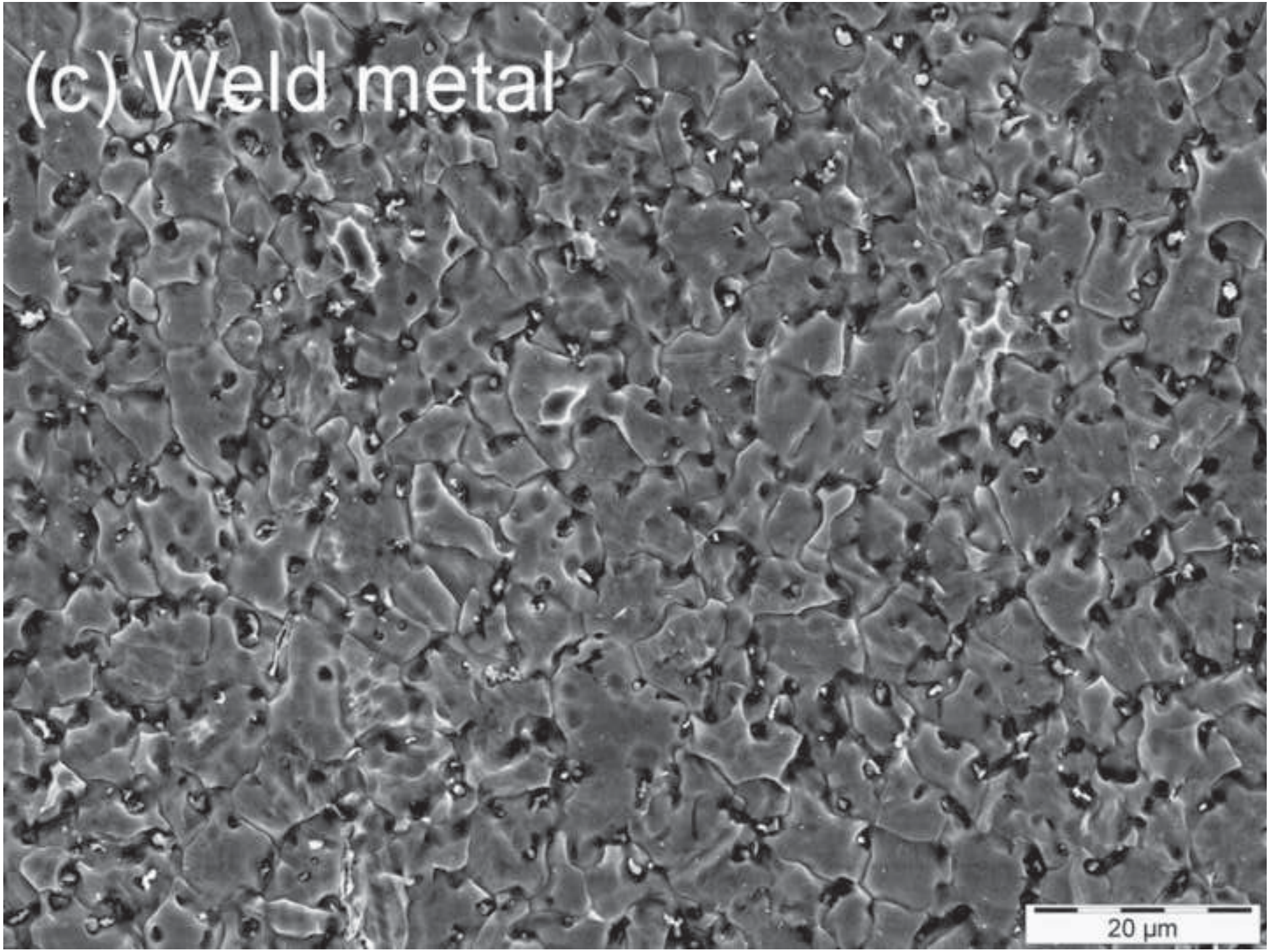

Figure 4a
Click here to download high resolution image

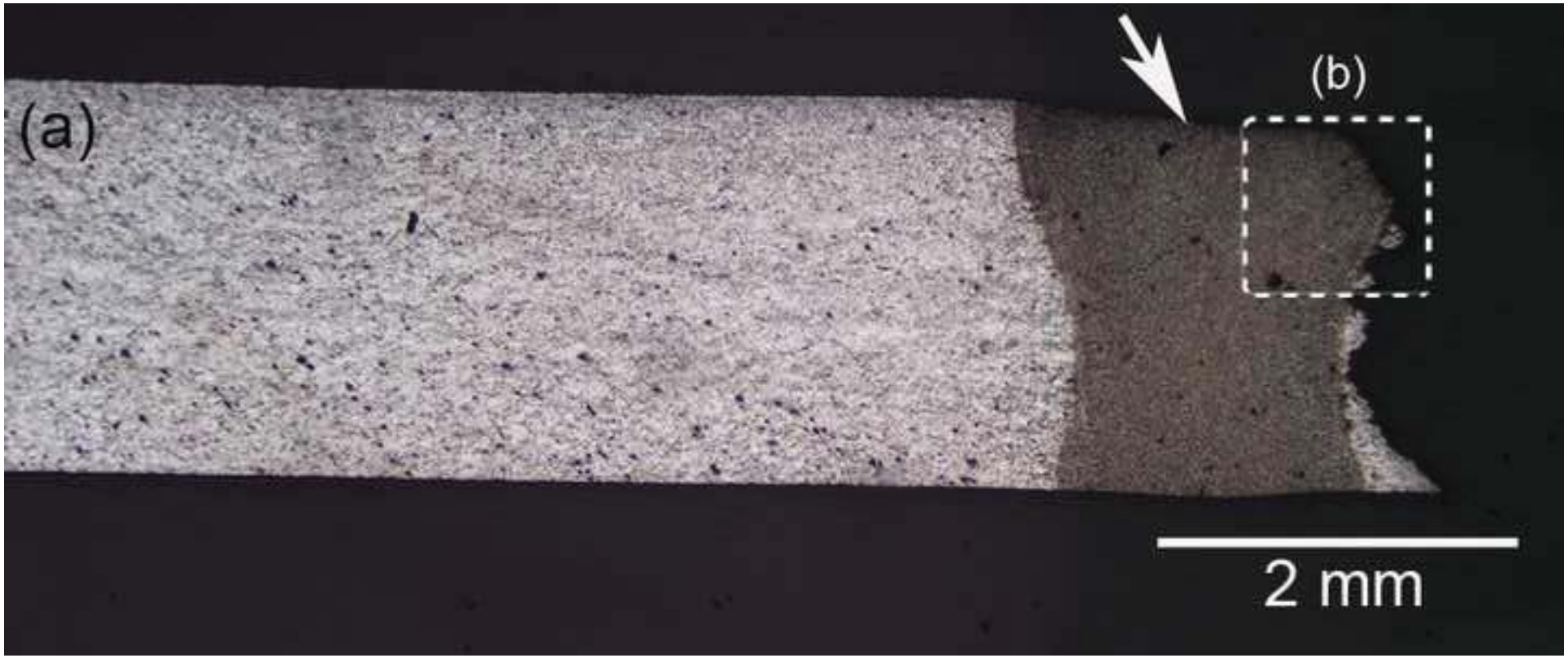

Figure 4b
Click here to download high resolution image

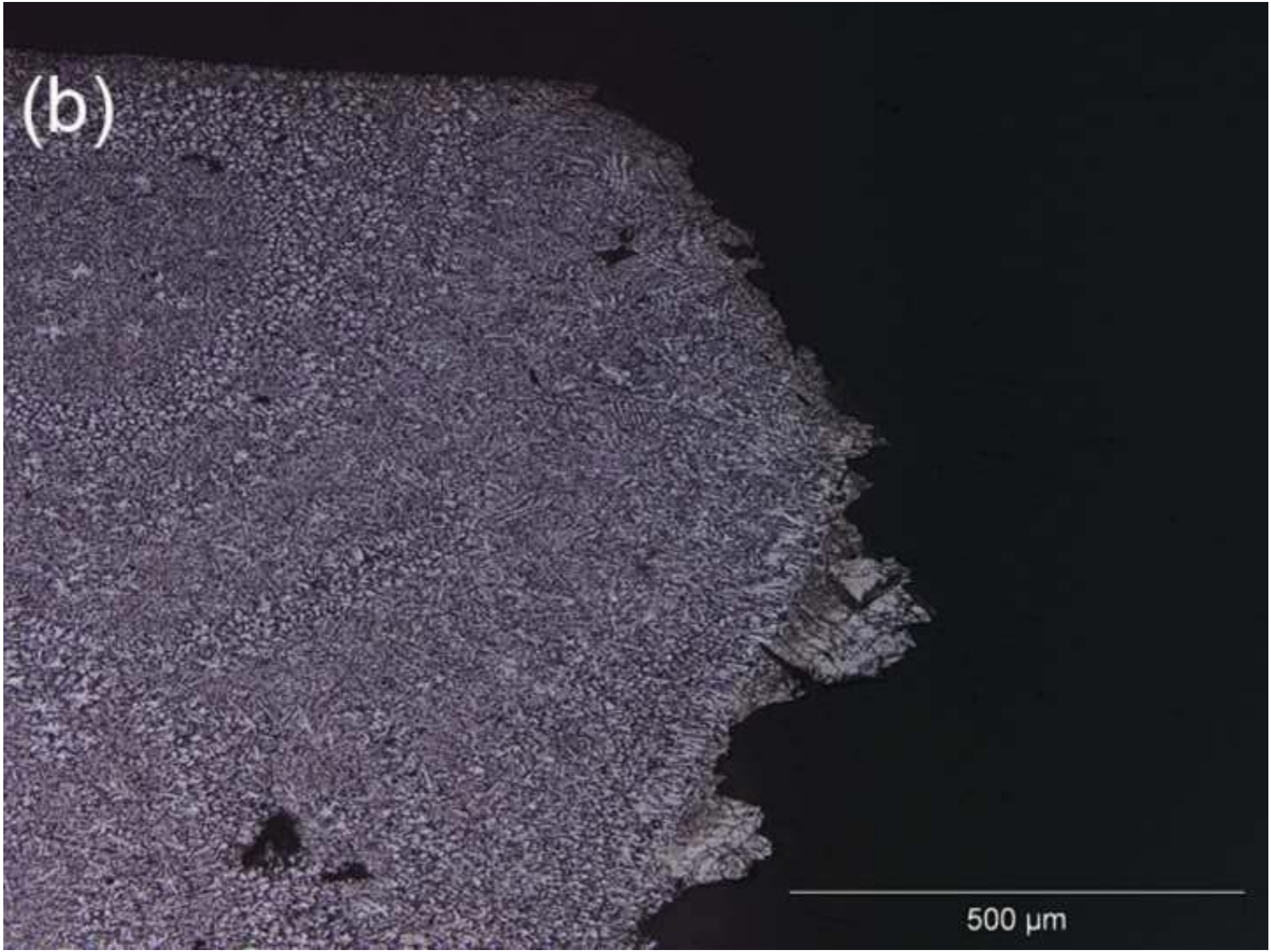

Figure 5a
Click here to download high resolution image

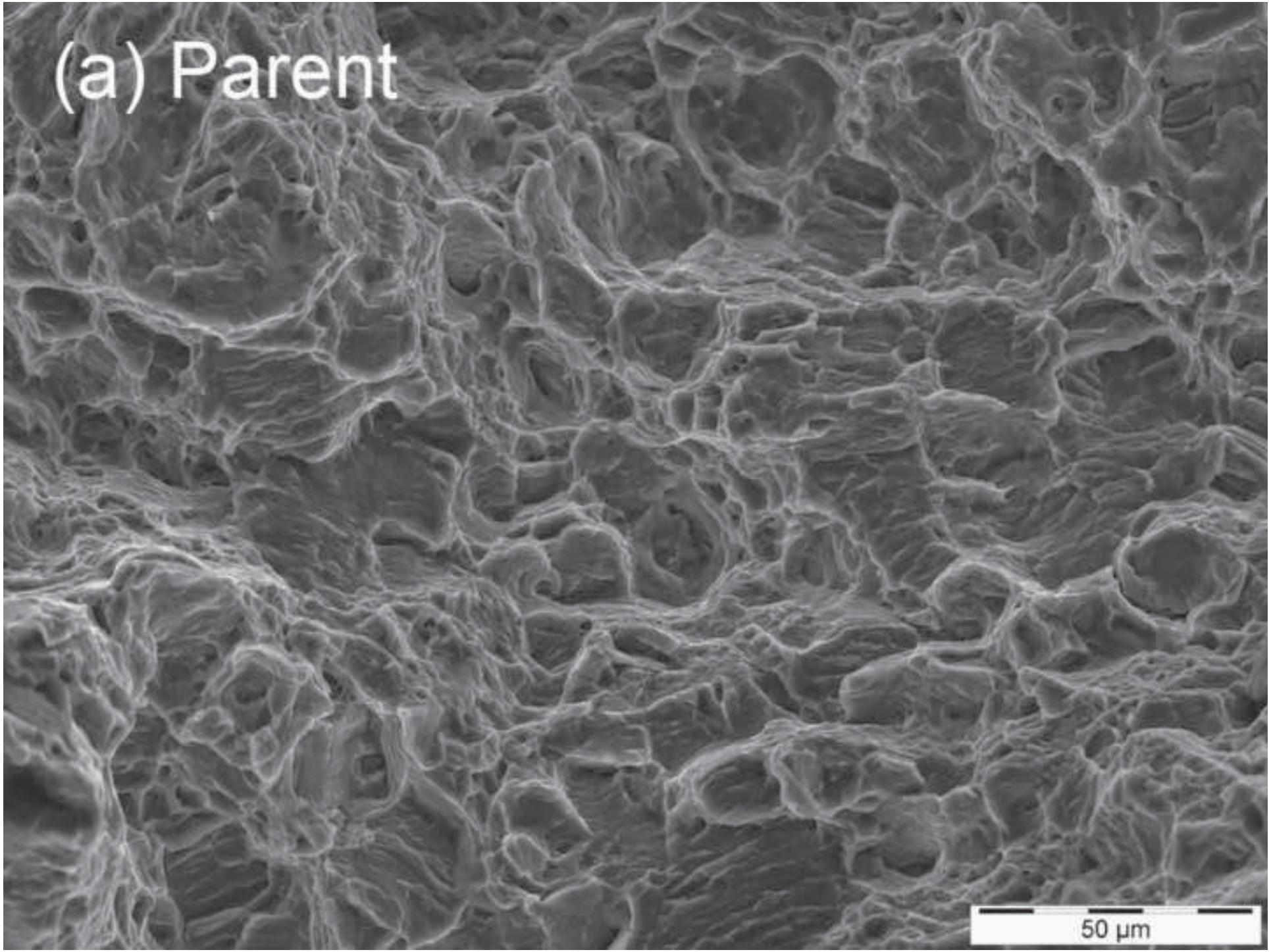

Figure 5b
Click here to download high resolution image

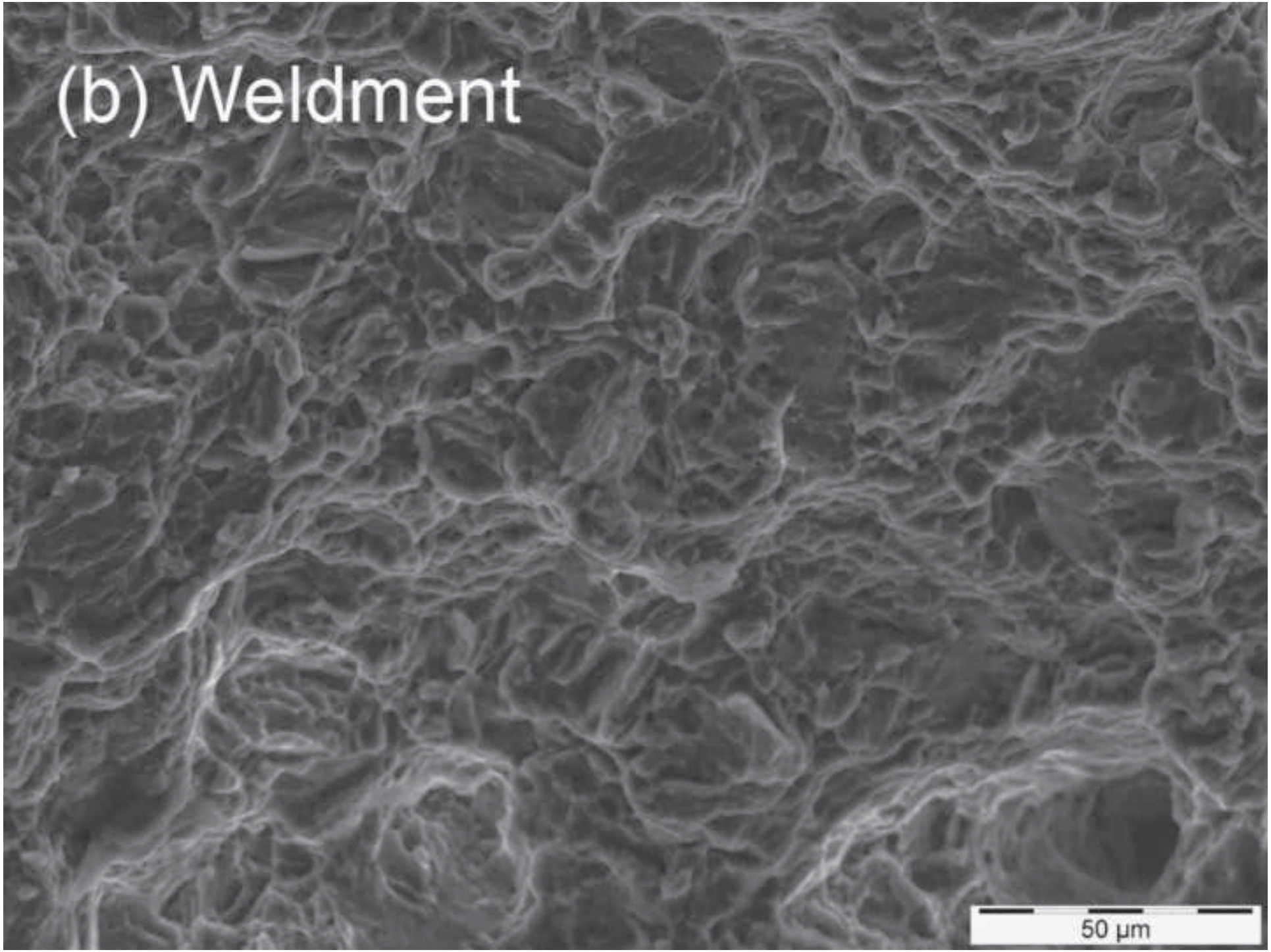

Figure 6a
Click here to download high resolution image

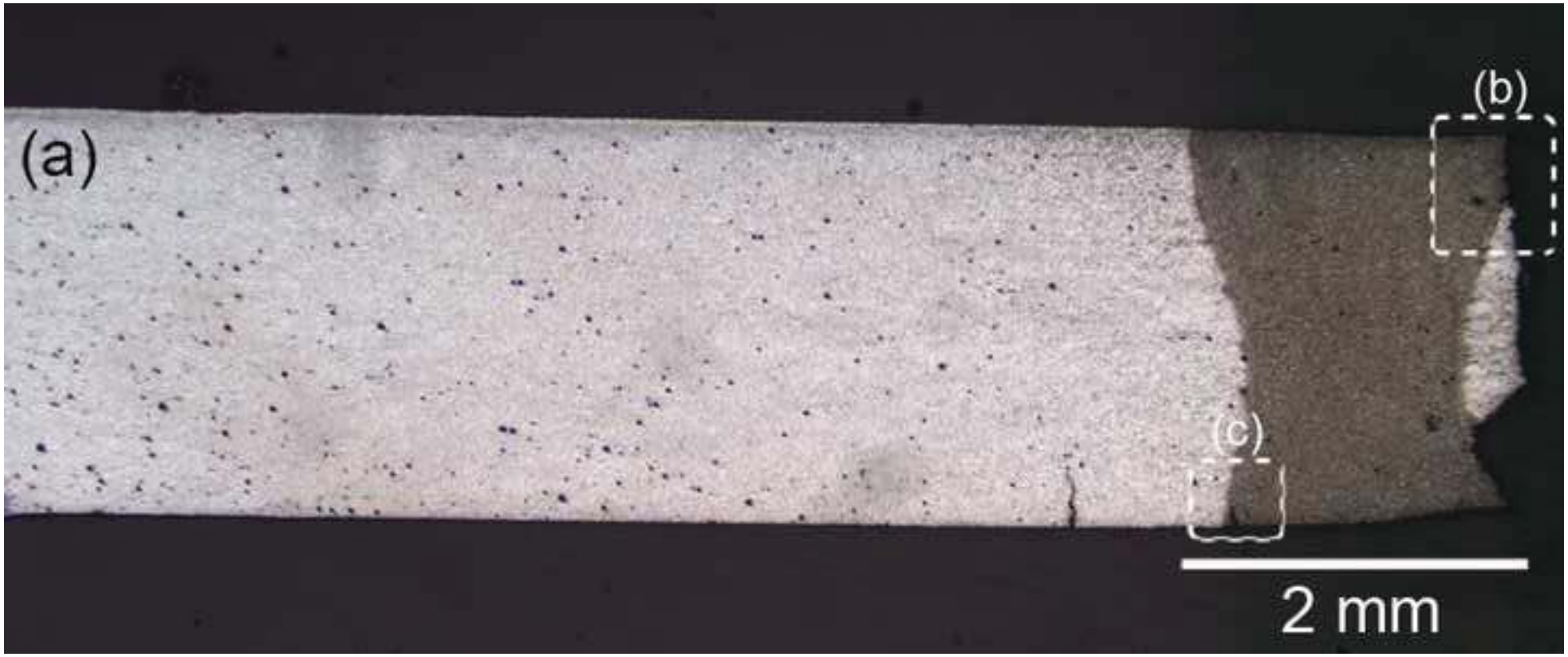

Figure 6b

Click here to download high resolution image

Figure 7a

Click here to download high resolution image

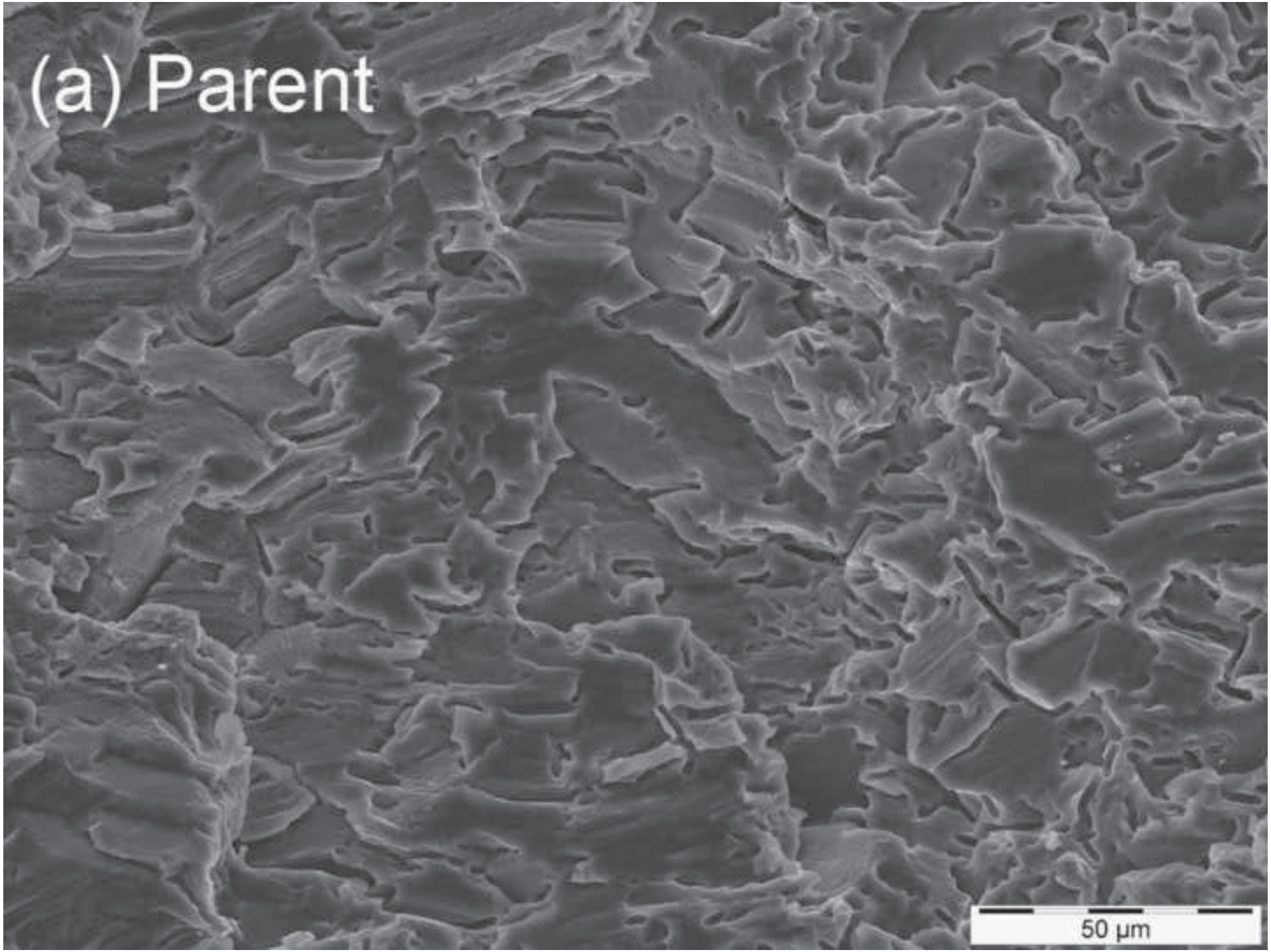

Figure 7b
Click here to download high resolution image

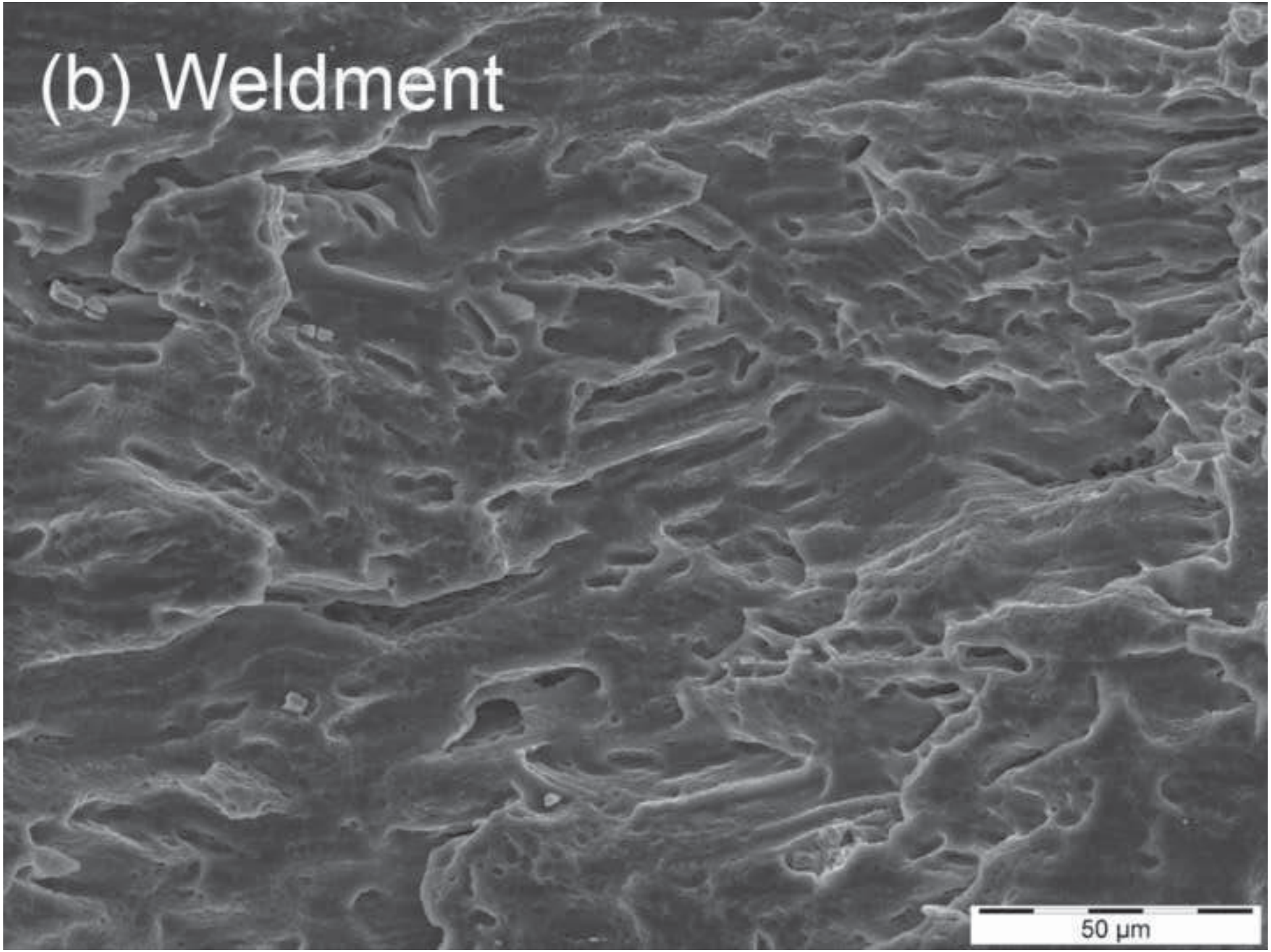

Figure 8

Click here to download high resolution image

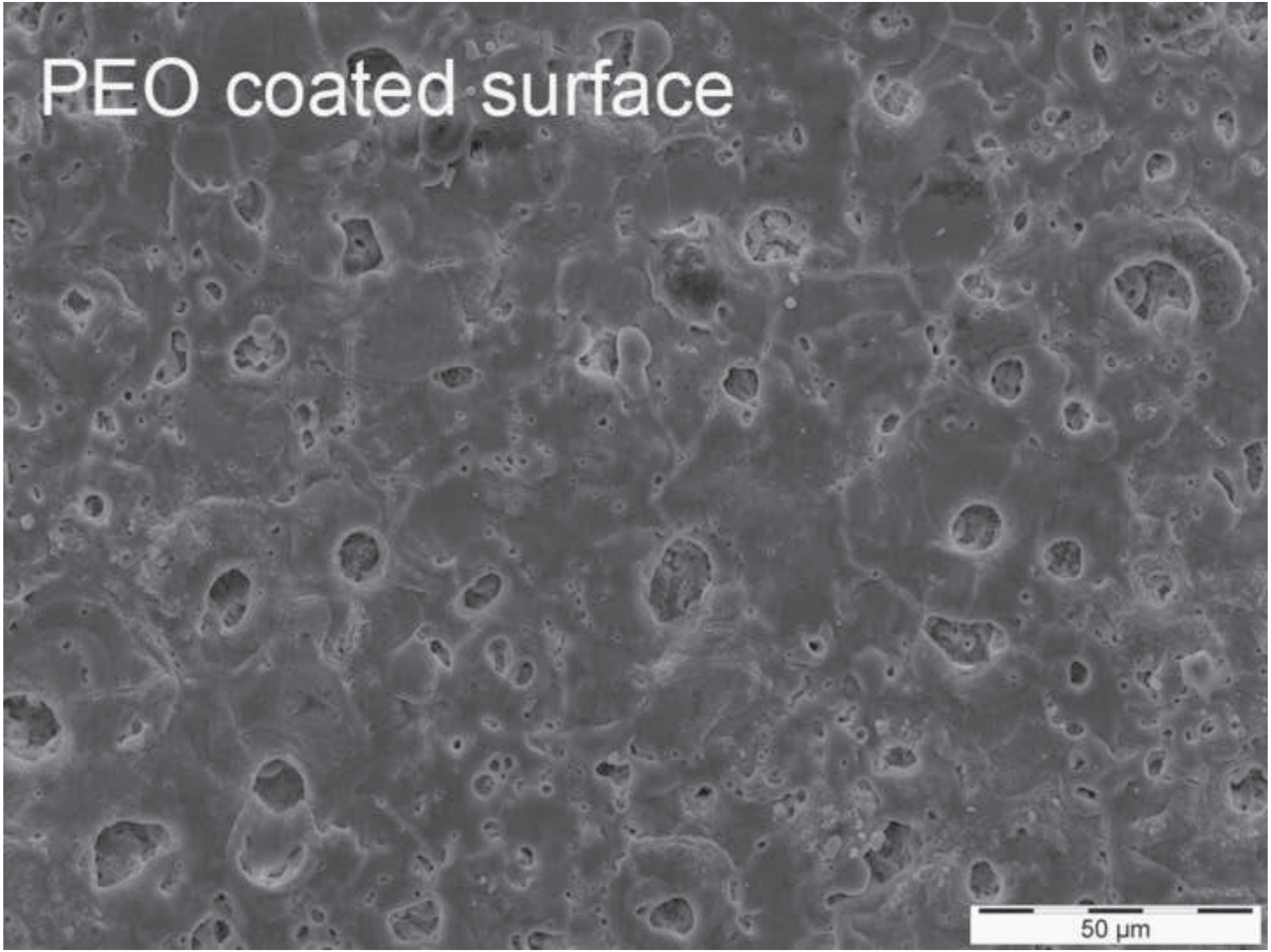

Figure 9
Click here to download high resolution image

Figure 10a
Click here to download high resolution image

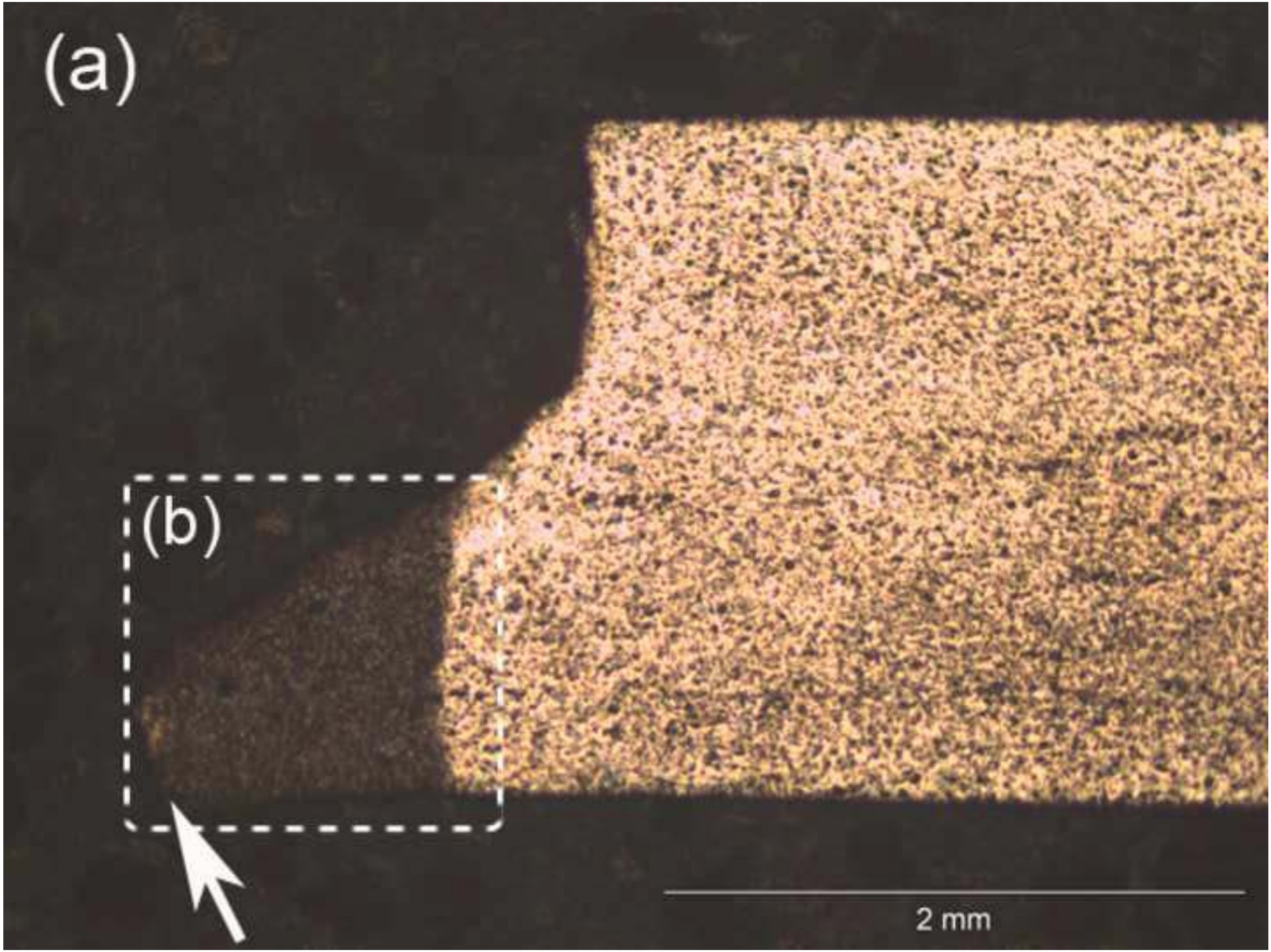

Figure 10b
Click here to download high resolution image

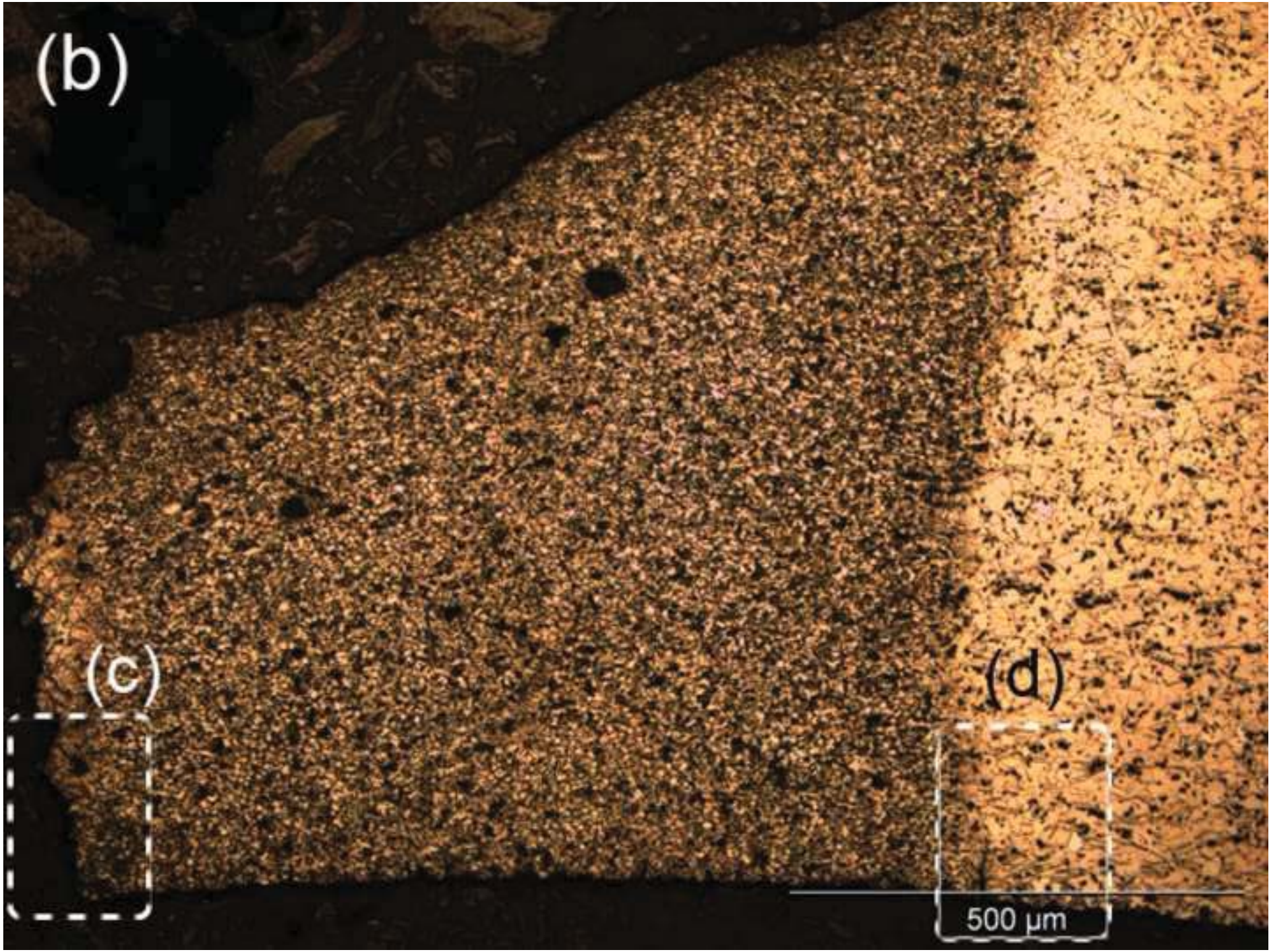

Figure 10c
Click here to download high resolution image

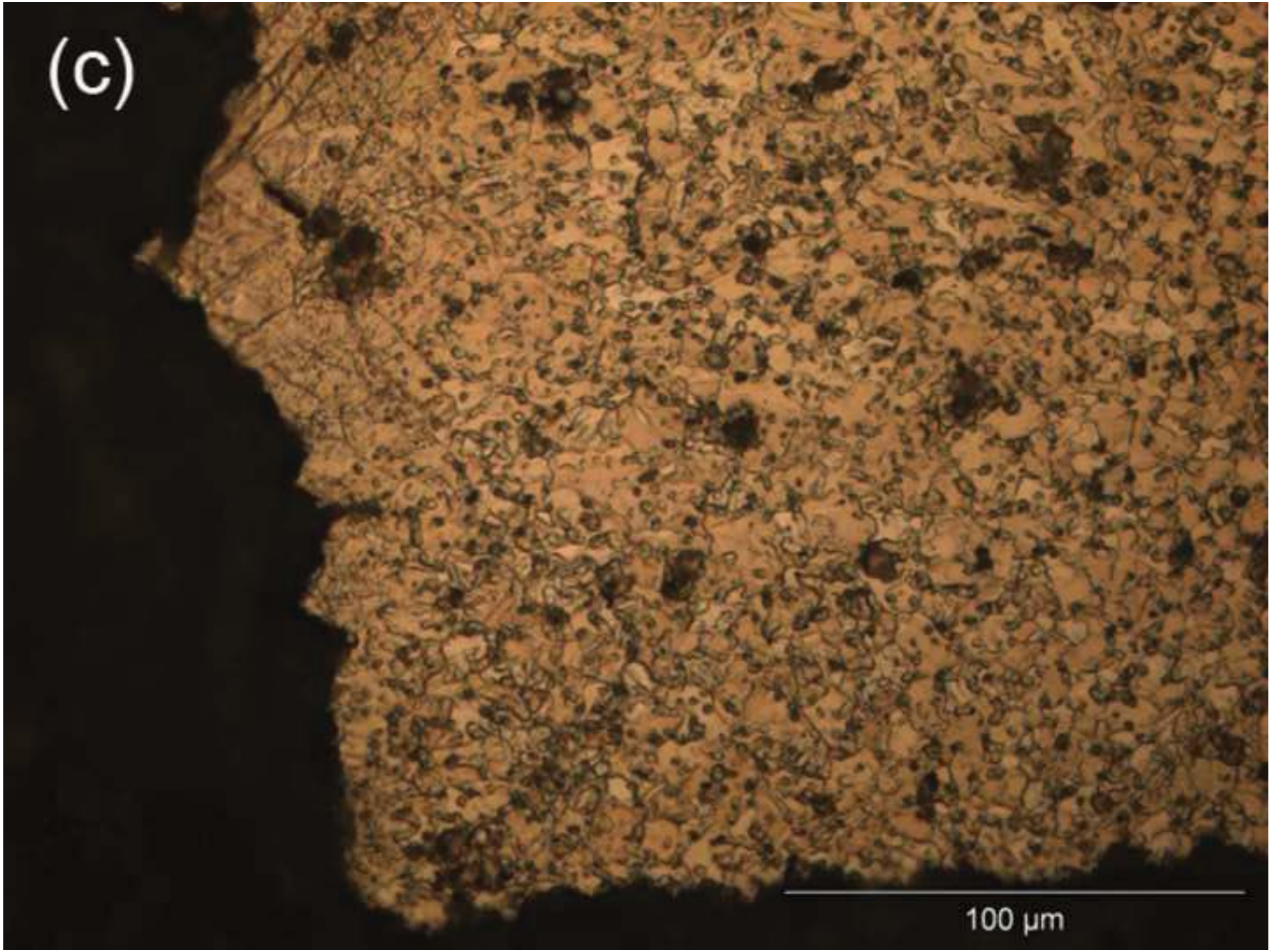

Figure 10d
Click here to download high resolution image

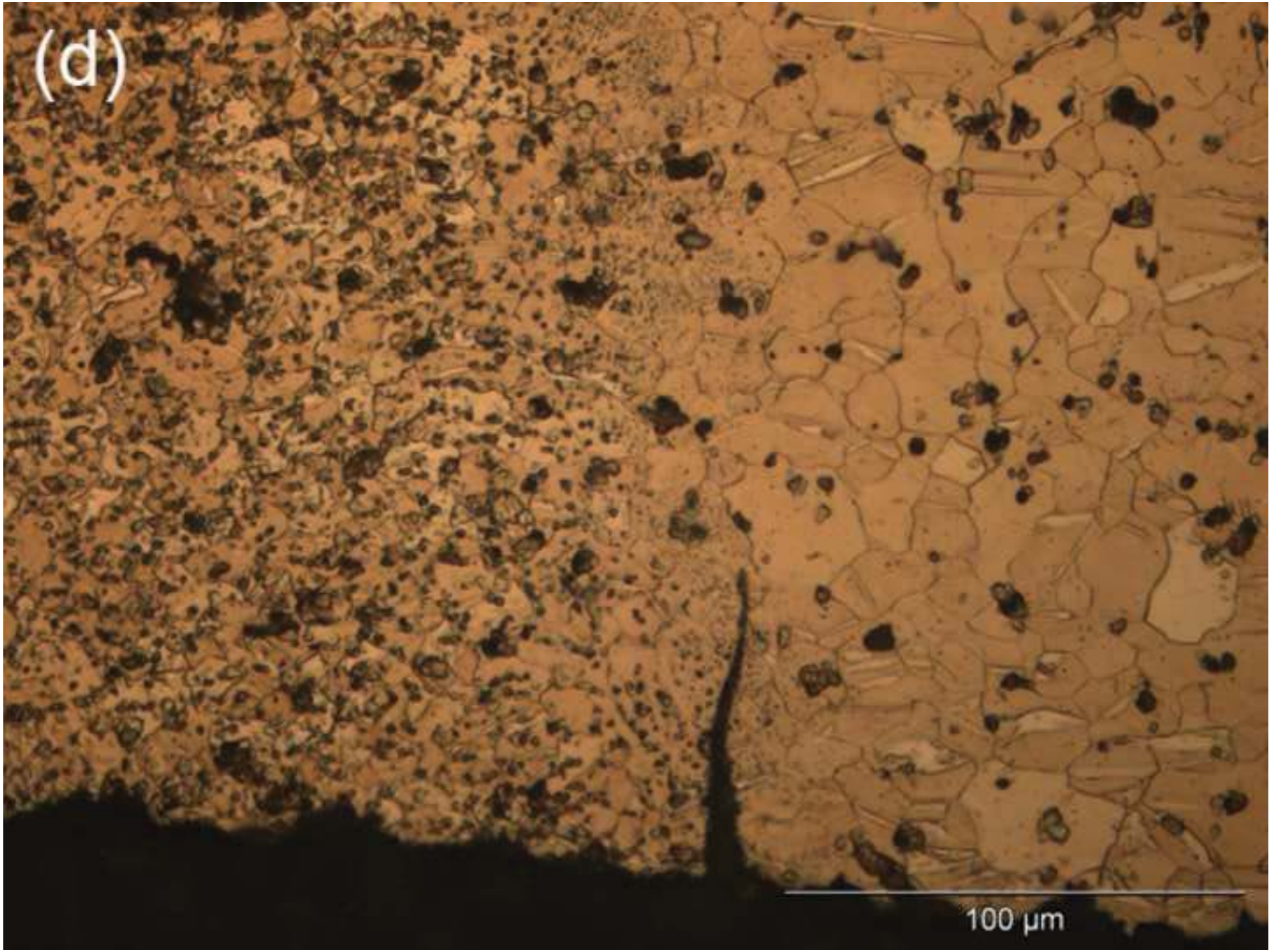

Figure 11
Click here to download high resolution image